Experimental Anaysis of Droplet Spatial Distribution in a Spray Burner

Olivier Rouzaud, Maxime Vicentini, Renaud Lecourt, Virginel Bodoc, Olivier Simonin

Experimental Anaysis of Droplet Spatial Distribution in a Spray Burner

Olivier Rouzaud*, Maxime Vicentini[1], Renaud Lecourt[2], Virginel Bodoc[1], Olivier Simonin[3]
[1]Aerodynamics and Energetics Modelling Dept., ONERA, Toulouse, FRANCE
[2]Aerodynamics and Energetics Modelling Dept., ONERA, Fauga-Mauzac, FRANCE
[3]Institut de Mécanique des Fluides de Toulouse (IMFT), Université de Toulouse, CNRS, INPT, UPS, Toulouse, FRANCE
*Corresponding author: rouzaud@onera.fr

Abstract
A new experimental setup has been built to study spray combustion. The design corresponds to a squared-duct channel with a bluff-body spanning over the entire width of the channel. Turbulent flow circulates around the obstacle and liquid fuel is injected at the rear of the body through a flat-fan nozzle. The two-dimensional configuration has been chosen to facilitate the optical measurements. Operating conditions reproduce partially those met inside a turboreactor.
Non-reacting and reacting flows have been experimentally characterized but the paper lays emphasis on the later case. Spatial distribution of the droplets has been investigated with respect to the inter-droplet distance to the nearest neighbour and to the spatial distribution law at six locations upstream of the bluff body. Inter-droplet distance is obtained through the processing of Mie scaterring data. For the distribution law, comparisons between the experimental distribution, the theoretical exponential distribution and numerical results from an in-house Monte-Carlo solver demonstrate that the droplet distribution is equivalent to the exponential distribution. Besides, the numerical approach has been used to estimate the errors associated with the inter-droplet distance.

Introduction

Gaseous combustion inside a combustion chamber has been studied for a long time due to its importance in industrial applications. However, spray combustion necessitates specific attention because injecting a liquid fuel inside a combustion chamber involves many different phenomena like liquid atomization, evaporation, formation of film on the chamber walls which are not present in the gaseous case. Amongst the different questions, a point of interest is to determine the global burning of a spray.

Starting from the works of Godsave [1] or Spalding [2] on the combustion of an isolated droplet of fuel, efforts have been done in the past on the theoretical, numerical or experimental grounds to answer this question [3]. In the eighties, different research groups developed theoretical models describing spray combustion [4, 5, 6]. For instance, Chiu and his co-workers proposed the concept of droplet group combustion, considering droplet cloud with monodisperse droplets arrayed at uniform intervals. The distance is deduced from the average density number of the cloud. They proposed a droplet group combustion diagram with four spray combustion regimes: the single droplet combustion, the internal group combustion, the external group combustion and the external sheath combustion. The regimes were classified through a group combustion number G:

$$G = 1.5\,\mathrm{Le}\left(1 + 0.276\,\mathrm{Sc}^{1/3}\,\mathrm{Re}^{1/2}\right) N^{2/3}\,d/D_i \tag{1}$$

where Le denoted the Lewis number, Sc the Schmidt number, Re the Reynolds number based on the droplet slip velocity, N the total number of droplets contained in the cluster, d the droplet diameter and D_i the mean distance between droplet centers. Since then, different group combustion diagrams have been proposed ([7, 8, 9]). Borghi proposes a description of spray combustion in a premixed flow based on Kerstein and Law model. The value $n^{1/3}\,r_F$, ratio between the flame radius around a single droplet and the uniform distance given by the droplet density number, depends on the ratio d/e_L, where e_L represents the flame thickness. For values $n^{1/3}\,r_F < 0.41$, droplets burn in group. For values $n^{1/3}\,r_F < 0.73$, pockets of gas are surrounded by flames. The intermediate case is a combination of the first two ones, in addition with the presence of a diffusion flame. Reveillon and Vervisch based their combustion diagram on some numerical simulations of a turbulent dilute-spray jet flame. Direct Numerical Simulation is used for the gaseous phase and a Lagrangian description for the spray. Particular attention has been paid to the influence of the equivalence ratio and of the dilute-spray density. Concerning the theoretical/analytical models, one can refer to the review paper of Annamalai and Ryan [3]. Droplet interactions has been studied for many different configurations from two droplets to arrays of droplets involving many different methods. One of the most interesting approach is the one proposed by Elperin and Krasovitov [10]. They considered random cluster of polydisperse droplets in evaporation or combustion, using an irreducible multipoles method. However, analytical models are also questionable since they usually rest on some simplifying assumptions like a uniform distance between droplets, gas

at rest or the constancy of the Lewis number $\mathrm{Le} = 1$.

On the experimental side, McDonell *et al.* [11] examined the structures of methanol sprays obtained by air-assist or pressure-swirl atomizer in non-reacting and reacting cases. Two-phase flow characterization is based on phase Doppler anemometry (PDA) and infrared extinction/scattering (IRES) method. In the case of swirling air-assisted spray, the analysis focuses on the differences between gas velocities, droplet velocities and diameters, and vapour concentration for both kind of flows. On their part, Akamatsu *et al.* [12, 13] worked on a premixed spray of kerosene droplet flowing through an annular burner. They performed simultaneous measurements of OH- and CH-light emissions, droplet Mie scaterring emission, droplet size and velocity using PDA. From their experimental data, Akamatsu and coworkers concluded that droplet clusters are present but, for many of them, the group combustion mode does not correspond to Chiu's classification. Indeed, some assumptions are not supported by the experimental spray as the sphericity of the cluster or the flow uniformity. More recently, Beck *et al.* studied the effect of incomplete droplet prevaporisation on NOx emissions in Lean Direct Injection systems [14, 15]. In this experiment, two liquid fuel injectors are used to control the degree of prevaporisation. The first one is far upstream the combustion chamber and generates a a fully prevaporized premixed incoming mixture. The second injector is located at the combustor inlet inside a swirl system enabling the aerodynamical stabilization of the flame. Spray characterization has been realised using 3D-phase Doppler and simultaneous CH-PLIF/droplet Mie scattering. Isolated droplets burn in the very dilute part of the flow under two possible regimes: an enveloppe flame surrounding the droplet or a wake flame behind the droplet. According to their numerical analysis, these regimes have a significant influence on NOx emissions. Finally, two-phase flow combustion has also been studied by Lovett *et al.* [16] in the framework of bluff-body stabilized flames for a non-premixed, jet-in-crossflow fuel injection. Results on the flame structure are discussed in relation to classical combustion reaction zone regimes. Experimental analysis is mainly based on chemiluminescence and planar fluorescence imaging (PLIF) of OH radicals to understand the development of the reactive zones with respect to the fuel injection or the upstream flow conditions.

This short review of the experimental studies shows that, although different aspects of spray combustion have been -and are still- addressed, constituting an exhaustive experimental database could be of primary importance for increasing our knowledge of such flows and for assessing numerical approaches. Thus, a new experimental device, the Prométhée-LACOM test rig, has been developed to study reacting and non-reacting two-phase flow [17, 18]. The configuration corresponds to a turbulent air flow circulating around a bluff-body in a square-duct channel. Liquid fuel is injected at the rear face of the obstacle and the bluff-body acts as a flameholder. The setup has been designed to facilitate experimental observations and to reproduce, at least partially, operating conditions of an aero-engine combustion chamber. The former constraint has been achieved by retaining a two-dimensional geometrical configuration, in accordance with the fact that most of the imaging techniques to be used are planar. Characterization of the non-reacting flow has been presented elsewhere [17] and the scope of the paper is thus limited to the reacting case. More particularly, emphasis is laid on the droplet spatial distribution, *i.e.* inter-droplet spacing and spatial distribution law. Droplet Mie scattering data have been used to estimate as local as possible values of the spray density number and of the mean nearest-neighbour inter-droplet distance at six different locations in the flow. The former value can be of interest for numerical validation while the droplet distance is considered as a key parameter in the spray combustion analysis, as previously quoted [4, 19]. Analysis of the experimental data has also been extended to the spatial distribution law. Comparison between the experimental data and existing laws tends to prove that the spray, although inhomogeneous, is organized according to the exponential distribution (Poisson process).

Material and methods

Test Setup

A new air-breathing propulsion test setup, Prométhée-LACOM, has been recently developed at ONERA (see Fig.1) to study spray combustion. The air feeding system is made up of a spherical pressure vessel (2.5 MPa), gas pressure regulators and an electric heater (1 MW). The air mass flow rate is measured with a sonic nozzle located downstream of the electric heater ($\pm$3.3% accuracy). Subsequently, the preheated air stream passes through a succession of flow conditioners and grids for generating turbulence. The test chamber consists of a square internal section (120 mm x 120 mm). The confined turbulent air stream flows around a fuel injection system prior to the combustion chamber. The injection system consists of a bluff-body in which a liquid fuel nozzle is mounted. The bluff-body spans over the entire width of the test section. The fuel feeding line (1.5 MPa) is equipped with a Coriolis flowmeter ($\pm$0.2% accuracy). The spray nozzle is centered and screwed into the rear face of the obstacle. A spray of droplets is generated downstream directly into the combustion chamber. The fuel injector corresponds to a flat fan nozzle which produces an elliptical-shaped polydisperse spray. The spray opening angles of the major and minor axis are respectively 150° and 25°. The wide angle is set up so as to spray towards the upper and lower walls of the combustor. The water-cooled combustor is equipped with three interchangeable UV-transparent windows allowing to perform optical measurements downstream of the injection system. Ignition of the air-fuel mixture is triggered by a hydrogen-oxygen torch. The burnt gases are ejected into the exhaust pipe.

A previous sizing study has been carried out on a prototype in 1:1 scale to choose the bluff-body geometry [17] under non-reacting conditions. For a 6 m/s inert bulk airflow velocity, at 298 K, a vortex-shedding phenomenon and

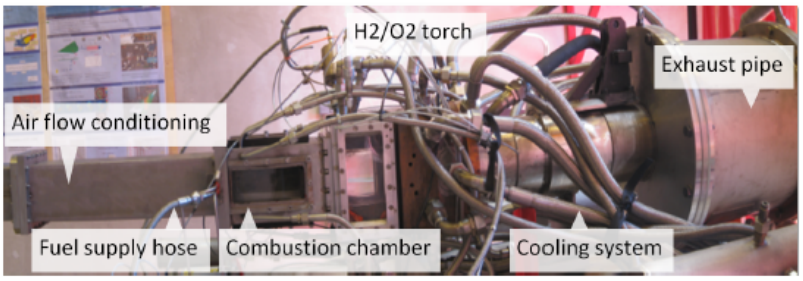

Figure 1. View of the test setup.

a large recirculation zone are observed downstream of the bluff-body. The criterion of choice for the bluff-body geometry and dimensions was based on the constancy of the Strouhal number and the intensity of the pressure signal measured on the bluff-body upper and lower faces with respect to the noise. As a result, a trapezoidal bluff-body with a 42% ratio blockage has been retained (Fig.2). Note that in reacting conditions, the von Kármán vortex street is no longer observed while the recirculation zone is still present.

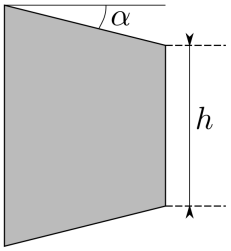

Figure 2. Geometry of the bluff-body.

Because of its bi-dimensional design, the experimental setup generates a turbulent flow with two-dimensional mean properties. Moreover, a large number of droplets is expected to be located around the vertical mid-plane of the combustor. Thus, since some of the experimental diagnostics used are planar (imaging devices), the configuration ensures the measurement of many relevant flow data (droplet positions, sizes, velocities and flame position). Furthermore, the setup reproduces partially the main features of the flow inside an actual aero-engine combustor. Indeed, the air flow is confined, turbulent and exhibits instabilities and large-scale structures. Besides, the flame is anchored aerodynamically by creating a main recirculation zone. The n-decane is selected as a surrogate fuel because it has chemical properties close to kerosene ones (density, surface tension, auto-ignition temperature). Furthermore, evaporation or chemical kinetics modelling are much simpler for a monocomponent fuel than for a mixture, should this configuration be calculated. The droplet spray is polydisperse with droplet sizes from 5 to 150 μm. Finally, the experiments replicate the operating lean-burn conditions of a turbofan engine, during a flight phase at cruising speed, in terms of fuel-air equivalence ratio.

Operating conditions

Although non-reacting and reacting two-phase flows have been investigated, we only consider reacting flow in this paper. The nominal operating point is set at an air mass flow rate equal to 64 g/s. At the combustor inlet, the air flow is at standard atmospheric pressure and 450 K. The corrected mass flow rate corresponds to 1.36 kg/s/bar/K$^{1/2}$. Since the combustion section is 120 mm x 120 mm, the bulk airflow velocity is close to 6 m/s. Consequently, the Reynolds number based on the hydraulic diameter is about 22 000. The liquid fuel temperature is measured just upstream from the nozzle and is equal to 330 K. The n-decane fuel (95% purity) is injected at 1 g/s to provide a 44 kW thermal power. Therefore, the fuel-air equivalence ratio is around 0.24. The water cooling of the combustion chamber protects the inner walls (T_{wall} < 650 K) and enables to perform tests lasting several tens of minutes.

Implementation of measurements

The main objective of this experimental programme is to build a spray combustion database for a better understanding of such flows and for the assessment of numerical approaches. In order to do so, gaseous and liquid phases have been studied in non-reacting and reacting conditions. Concerning the reacting conditions, one employs OH-chemiluminescence, OH-Planar Laser-Induced Fluorescence (OH-PLIF) imaging, droplet Mie scattering and Phase Doppler Interferometry (PDI) technique to characterize the flow. Chemiluminescence and PLIF imaging are employed to study the flame fronts. The first technique uses spontaneous chemical excitation of a flame marker unlike the second technique, where excitation of the marker is produced by means of a laser. Droplets illuminated by a laser sheet generate light Mie scattering. This signal is captured by a camera in order to evaluate the positions of droplets from Mie images. Simultaneous OH-PLIF and Mie scaterring measurements provide instantaneous informations about the droplet spatial distribution with respect to the reacting zones. Finally, application of a two-component PDI allows to measure the instantaneous droplet velocities (longitudinal, transverse) and their sizes. Except the OH-chimiluminescence which is a three-dimensional technique, all the measurements have been performed in the vertical mid-plane of the combustor.

Fig.3 presents the optical system for both OH-PLIF and Mie scattering techniques. Due to the scope of the paper, we only give details on the Mie scattering setup. To illuminate droplets, a millimetric thin visible laser sheet is produced from the outlet of a high-frequency Nd:YLF laser Quantronix Darwin (λ = 527 nm) using a cylindrical lens. The visible laser sheet crosses the combustion chamber from the bottom window. The frequency of the system is fixed to 1 kHz with a laser pulse around 200 ns. A high-speed camera Phantom V341 is positioned aside to capture the Mie scaterring signal from the droplets through a lateral window of the combustor. Light intensity is equal to 12 bits/pixel and the associated levels vary from 0 to 4095. Window maximal resolution is 2560 pixels x 1600 pixels. In the sequel, analysis of Mie scaterring is performed in six specific regions of the flow, considering only small parts of the overall Mie image (Tab.1). Such a choice enables to get a relatively local characterization of the spray.

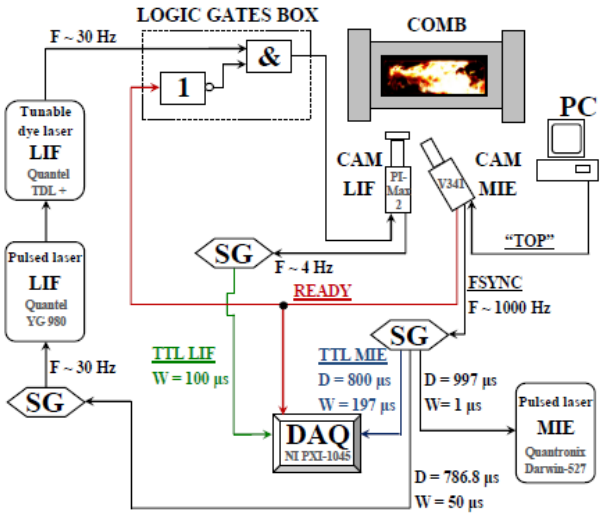

Figure 3. Setting and digital timing diagram for the synchronization of OH-PLIF and Mie scattering imaging.

Results and Discussion

Fig.4 presents the system of coordinates and the locations of the analysis windows defined later. The (X,Y) coordinates correspond respectively to the longitudinal and transversal axis, and are in the vertical mid-plane of the combustor. The origin of the frame of reference is on the lower wall of the channel. It is vertically aligned with the rear face of the bluff body. The centre of the injection system is at coordinates (0,60) in millimeters. Downstream of the obstacle, one can see two OH-PLIF images taken in the upper part and in the lower part of the flow but not at the same instant. They have been assembled for a better understanding of the flow.

Fig.4 also indicates the position of the six windows of analysis that has been chosen to study the droplet spatial distribution more precisely, using Mie scattering images. The coordinates of the center of gravity of the six windows are given in Table.1. Three points are located in the upper part of the channel above Y=60 mm and the others in the lower part. The table also specifies the sizes of the analysis windows in micrometers. These sizes have been chosen in order to provide statistical data on the spray distribution as local and as accurate as possible. The local constraint means that the size of the window should not be too large to define values representative of the local spray distribution. The accuracy property prescribes to have a sufficient number of samples (droplet positions) to

perform reliable statistics.
The experimental work presented hereafter is split in two parts. The first part of the work deals with the experimental analysis of the centre-to-centre inter-droplet distance to the nearest neighbour since this value is commonly considered in evaporating or reacting sprays to characterize droplet interactions. In the sequel, this distance will be simply called inter-droplet distance and written D_i. In a second time, the spray distribution law is investigated and compared to existing laws.

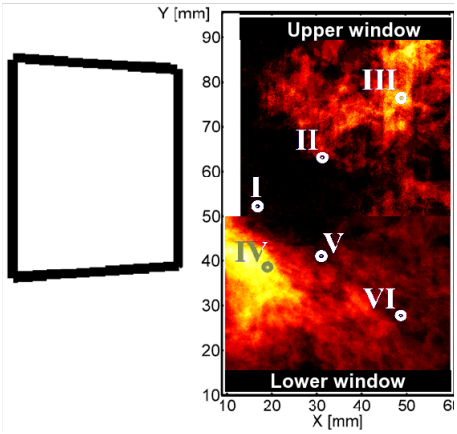

Figure 4. Frame of reference and positions of the window analysis.

Droplet spacing
Experimental analysis of the inter-droplet distance
For each analysis window, we have at our disposal $L^R = 2\,000$ images. Several steps are necessary before performing a statistical analysis on the inter-droplet distance. At first, Mie scattering images have been treated to suppress the soot luminance and the out-of-scope particles. To meet the first objective, one employs a smoothing procedure based on sliding-window algorithm (size 16 pixels x 16 pixels). This procedure acts as a linear low-pass filter on the luminance intensity. Concerning the out-of-scope particles, one defines a threshold value for the light intensity (value of 85 out of 4 095 levels, in our case) and retains the droplets with intensity above this level.
The second step consists in determining the mean density number of particles $\bar{n}$ in the analysis window. By denoting N^R the number of particles in each image R, the associated density number per unit surface n^R is straightforwardly given by:

$$n^R = \frac{N^R}{\text{Window area}}, \tag{2}$$

leading to the definition of the mean density number

$$\bar{n} = \frac{1}{L^R} \sum_{R=1}^{L^R} n^R \tag{3}$$

Table 1. Centers and sizes of the analysis windows.

Window	Coordinates (mm)	Window size (μm^2)
I	(17, 52)	993$\times$ 993
II	(31, 63)	3319$\times$3319
III	(49, 76)	5673$\times$5673
IV	(19, 39)	2837$\times$2837
V	(31, 41)	1986$\times$1986
VI	(49, 28)	5673$\times$5673

Determination of the inter-droplet distance constitutes the next step. For each droplet S in an image R, its center of gravity is deduced from the first-order moment integral of its pixel coordinates according to

$$\begin{cases} X^{R,S} = \dfrac{1}{A(X,Y)} \displaystyle\int\int_{\mathcal{D}} X \, dX \, dY \\ Y^{R,S} = \dfrac{1}{A(X,Y)} \displaystyle\int\int_{\mathcal{D}} Y \, dX \, dY \end{cases} \tag{4}$$

where $A(x,y)$ is the droplet area. The inter-droplet distance $D_i^{R,S}$ for the S-th droplet of the R-th image is the minimal value of the Euclidean distance between the S-th droplet and all the other droplets belonging to the same image, *i.e.*:

$$D_i^{R,S} = Min\left(\sqrt{(X^{R,S} - X^{R,S*})^2 + (Y^{R,S} - Y^{R,S*})^2}\right), S* \in \left[1, N^R\right] \setminus S \tag{5}$$

Once all the Mie images have been treated, the mean value and the standard deviation of the inter-droplet distance for the analysis window under consideration are evaluated as

$$\mathsf{E}\left[D_i\right] = \frac{1}{L^R N^R} \sum_{R=1}^{L^R} \sum_{S=1}^{N^R} D_i^{R,S} \tag{6}$$

and

$$\mathsf{SD}\left[D_i\right] = \sqrt{\frac{1}{L^R N^R} \sum_{R=1}^{L^R} \sum_{S=1}^{N^R} \left(D_i^{R,S} - \mathsf{E}\left[D_i\right]\right)^2} \tag{7}$$

The same procedure is adopted for all the analysis windows.

Table 2 summarizes the main results obtained at the six points under consideration. Starting from the second column, the data yield the number of samples, the mean density number $\bar{n}$, the mean inter-droplet distance $\mathsf{E}\left[D_i\right]$ and its associated standard deviation $\mathsf{SD}\left[D_i\right]$, a so-called uniform distance D_i^{unif} and the distance parameter $\bar{C}$. The last value corresponds to the ratio of the inter-distance droplet to the local mean arithmetic diameter d_{10}. The regular distance D_i^{unif} is calculated as if the droplets were uniformly arrayed inside the window. By definition, this distance writes as

$$D_i^{unif} = \frac{1}{L^R} \sum_{R=1}^{L^R} \left[n^R\right]^{-1/2} \tag{8}$$

Such a distance is often used to underline the neighborhood effects between droplets in evaporation or in combustion, involving ratios between this distance and the droplet diameter or the flame diameter around a droplet. According to [19], there is no interaction between two droplets for a distance parameter C above 10. In most aeronautical combustion chambers, the value of this parameter is between 5 and 40 [5, 7].

A first comment bears on the evolution of the mean density number and the mean inter-droplet distance. According to the data, the mean density number varies from a larger value close to the flat fan injection (point I) to smaller values far away (points III and VI). Such an evolution is consistent with the presence of the flame involving high-temperature and a more rapid evaporation of the smaller droplets compared to the non-reactive case. For instance, there is a factor 20 in the density number at point III between the non-reacting and reacting cases. Note also that the quite dense spray at point I precludes the flame penetration close to the injection system as revealed by the Mie-PLIF superimposed images. The mean inter-droplet distance values are consistent with the mean density number behaviour. In particular, it increases with the distance to the injection system. Referring to the distance parameter in the last column, we note that the spray evolves between droplet interactions and isolated droplet behaviours according to the admitted description [19].

Secondly, one compares the inter-droplet distance to the regular one. In all cases, the experimental values are smaller than the regular values with a factor varying between 1.3 and 2. Thus, in this experiment, the regular distance is not the most representative distance for droplet interactions.

Size of the analysis windows

Since we intend to determine values of the droplet density number as local as possible, the size of the windows should be small with respect to the overall Mie image. On the other side, performing a statistical analysis on the inter-droplet distance D_i requires to consider a sufficient number of samples (droplets). Due to the spray inhomogeneity, the trade-off between these two constraints leads to choose different sizes according to the window locations (Table 3).

Influence of the window size has been studied. For instance, in the case of window I, Table 3 gathers the mean density number, the mean nearest-neighbour distance and the associated standard deviation for three different sizes of the analysis window from simple to double. The differences between the values are limited and the intermediate window has been retained as seen in Table 1. Similar analysis have been realized for the other locations.

Droplet spatial distribution law

To get further insight in the spray organization, we now try to characterize the spatial distribution of the droplets in each analysis window by comparison with the uniform (droplets arrayed at uniform intervals) and the exponential distributions. Given a mean surfacic density number $\bar{n}$, the inter-droplet distance between nearest neighbour writes, in the case of the uniform distribution, as

$$D_i^{unif} \, = \, \bar{n}^{-1/2} \tag{9}$$

Concerning the exponential or Hertz-Chandrasekhar distribution, one can demonstrate [20] that the mean distance and its standard deviation are expressed as

$$\mathrm{E}\left[D_i^{H-C}\right] \, = \, 0.5\,\bar{n}^{-1/2} \quad ; \quad \mathrm{SD}\left[D_i^{H-C}\right] \, \approx \, 0.2613\,\bar{n}^{-1/2} \tag{10}$$

Since the experimental values of the density number depends on time, making comparisons with the two previous theoretical laws imply to retain the Mie images of which the density number is close to the mean value $\bar{n}$. In this work, the selection criterion is fixed to $\pm$10%, meaning that we retain images for which $n \in [0.9\bar{n},\, 1.1\bar{n}]$. The mean distance and standard deviation of both theoretical and experimental distributions are respectively plotted in Fig.5 left and Fig.5 right for the six windows of analysis. The extremal values of the mean density number correspond to the windows for which the spray is respectively the less or the more dense. These comparisons demonstrate that the experimental distributions are much closer to the Hertz-Chandrasekhar distribution than to the uniform one in any case. The evolution of the mean distance can be approximated as a straight line according to

$$\mathrm{E}\left[D_i|\bar{n}\right] \, = \, \alpha\,\bar{n}^{-1/2}, \tag{11}$$

with α equal to 0.59, a value to be compared to 0.5 for the exponential distribution and 1 for the uniform one. The same remark can be made for the standard deviation with a β-slope equal to 0.36 for the experimental data and equal to 0.26 for the Hertz-Chandrasekhar distribution. Note that the slope of the uniform distribution is null by definition.

Consider now the experimental processing of Mie images. It relies on a projection step from a three-dimensional slab towards a two-dimensional image, followed by a restriction step from a large image to a small image (Fig.6). We assume that these two steps are responsible for the discrepancies between the distributions. Validation of this assumption led to the development of a Monte-Carlo software tool where droplets are randomly placed in a cube according to the Hertz-Chandrasekhar distribution. The number of droplets is defined by the volume and a three-dimensional density number $\bar{n}_l$ correlated to the experimental surface density number $\bar{n}$. For instance, consider the first window of which the side i equal to l. The droplets experimentally observed in a Mie image are, in fact, located in a sheet of thickness ϵ equal to 1 mm. Conservation of the number of droplets between the two-dimensional Mie image and the three-dimensional volume gives the following relation between the density numbers

$$\bar{n}_l\,\epsilon\,l^2 \, = \, \bar{n}\,l^2 \tag{12}$$

Once the equivalent density number is defined from the mean density numbers given in Table 3, one places droplets inside a volume and we select a volume element of sides l and thickness ϵ. From that point on, the process is completly equivalent to the experimental one. For each selected volume (each Mie image), the droplets are projected on

Table 2. Outcomes of the experimental distributions of droplets.

Window	Nb. samples	$\bar{n}$ (cm^2)	$E\left[D_i\right],\, SD\left[D_i\right]$ (μm, μm)	D_i^{unif} (μm)	$\bar{C} \, = \, E\left[D_i\right]/d_{10}$
I	38 000	1 929	(178, 61)	227	4
II	56 100	258	(365, 217)	623	9
III	27 900	44	(860, 721)	1507	22
IV	33 900	215	(387, 245)	682	9
V	37 600	477	(248, 148)	458	7
VI	76 300	120	(503, 331)	913	12

a plane, the inter-droplet nearest-neighbour distances are calculated and statistical analysis is performed as previously. The associated results are presented on both images of Fig.5 as "Random(simulation)". They are in-between the theoretical and the experimental curves but closer to the latter ones as confirmed by the slopes values. Such results demonstrate that the experimental distribution is equivalent to the exponential distribution. The Monte-Carlo solver will be used in the next paragraph to evaluate the error committed on the inter-droplet distance.

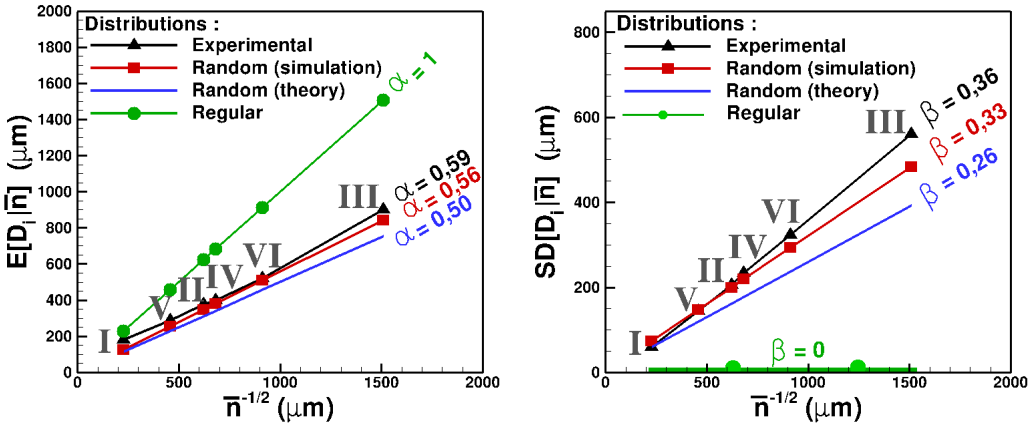

Figure 5. Variation of the conditional average inter-droplet distance and the standard deviation vs the inverse square root of the density.

Error analysis

To estimate the quality of our results on the droplet spacing or the spatial distribution, evaluation of two different errors has been performed. The first one is associated with the transformation of Mie images into binary images. The accuracy of the images is 35.2 pixel per millimeter, *i.e.* one pixel corresponds to 28 micrometers. Thus, the error committed on the gravity center coordinates of any droplet is expected to be around 20 μm. Since the coordinates of two droplets are used to calculate their inter-droplet distance, the error on this distance in the worst case is around 40 μm. Referring to Table.2, the relative error varies between 4.5 and 22 %.

Consider now the errors associated with these two steps, respectively called projection and restriction errors (Fig.6). To assess their importance on the inter-droplet distance, a Monte-Carlo numerical approach has been employed. Numerical droplets are randomly dispersed inside a slab volume of which the dimensions are equivalent to the dimensions of the experimental Mie images. Besides, density numbers are taken from the experimental values. The statistical analysis of the Monte-Carlo data follows the same procedure than the experimental one. The projection step consists in projecting the droplets on the (X,Y) plane, discarding the third coordinate. The inter-droplet distance is then calculated for both three-dimensional and two-dimensional distributions, and the comparisons of these two values provide an indication of the projection error. In the next step -the restriction one-, the large two-dimensional numerical image is split into a set of smaller images of which the sizes are comparable with the sizes of the analysis windows. Comparison of the inter-droplet distance for the large image and the set of the smaller images provide an estimation of the restriction error. This difference is due to the fact that, for some droplets located in the border zone of an image, its nearest-neighbour droplet is out of the image. Such a border zone effect [21] is all the more important as the size of the image is smaller.

Table 4 summarizes the projection and restriction errors for the six analysis windows. The total error estimation corresponds to their product. As expected, the projection step decreases the inter-droplet distance. The projection error is all the more important as the side length of the window is comparable to the thickness of the measurement volume. Possible improvements would be to reduce the laser sheet thickness or to extend the window size. In that case, it would be at the expense of a localized measurement. On the other side, the restriction effect overestimates

Table 3. Influence of the size of an analysis window.

Window size (μm^2)	Nb. samples	Mean density number (cm^2)	E $[D_i]$ (μm)	SD $[D_i]$ (μm)
709 x 709	20 270	2 016	183	64
993 x 993	38 000	1 929	178	61
1 390 x 1 390	74 200	1 920	171	58

the inter-droplet distance because of the border zone effect. Minimizing the error would be possible by using the neighbouring Mie images to remove the droplets submitted to the border zone effect.

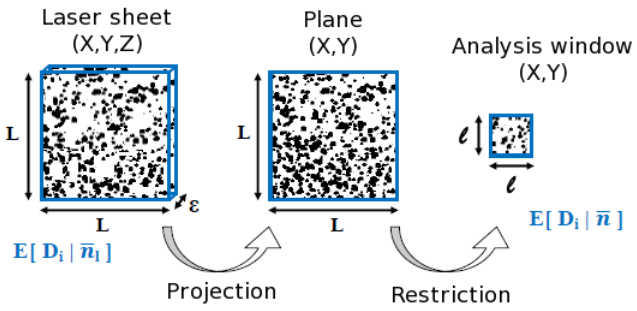

Figure 6. Description of the data processing for the error analysis.

Conclusions

A new experimental setup (Prométhée-LACOM) has been designed to study spray combustion and provide an experimental database to acquire a better knowledge of such flows and for further assessment of the numerical approaches. The setup consists of a trapezoidal bluff-body located inside a square-channel duct. The upstream air flow is turbulent and liquid n-decane is injected at the rear face of the bluff-body with a flat-fan atomizer. Operating conditions reproduce partially the conditions met inside an aero-engine combustor.

Measurements have been done for both non-reacting and reacting cases to describe the gaseous and the liquid phases. In the paper, emphasis is laid on the spray distribution in the reacting case. At first, using Mie scaterring from droplets enabled to estimate as local as possible values of the droplet density number in six regions of the flow and to derive values of the inter-droplet distance between nearest-neighbour particles. This distance is believed to be an important parameter since it is often used to characterize droplet interactions by comparison with the droplet diameter or the droplet flame diameter. Further data analysis also shows that droplets are randomly dispersed according to the exponential distribution.

Further insight in spray combustion behaviour will necessitate to perform additional measurements and to support the experimental observations with numerical simulations. At the time being, a partial validation of ONERA industrial solver CEDRE has already been achieved in the non-reacting case [22].

Acknowledgements

The work has been realized thanks to the partial financial support of the "Région Midi-Pyrénées". The authors would also like to thank F. Bigot for his invaluable involvement in the manufacturing of the Prométhé-LACOM setup.

Nomenclature

$\mathrm{A(X,Y)}$	droplet area [$\mu\mathrm{m}^2$]
C	distance parameter [-]
d	droplet diameter [μm]
$\mathrm{d_{10}}$	mean droplet diameter [μm]
D_i	inter-droplet distance [μm]
D_i^{H-C}	inter-droplet distance from Hertz-Chandrasekhar distribution [μm]

Table 4. Estimation of the inter-droplet distance errors.

Window	Projection error	Restriction error	Total error estimation
I	-45%	+10%	-39%
II	-22%	+ 8%	-16%
III	-4%	+21%	+16%
IV	-20%	+11%	-12%
V	-31%	+10%	-23%
VI	-12%	+ 7%	- 6%

$D_i^{R,S}$	inter-droplet distance for the droplet S in image R [μm]
D_i^{unif}	inter-droplet distance from uniform distribution [μm]
$E[D_i]$	mean value of the inter-droplet distance [μm]
G	Chiu's group combustion number [-]
Le	Lewis number [-]
L^R	number of Mie images per analysis window [-]
l	size of an analysis window [μm]
N	total number of droplet inside a cloud [-]
N^R	number of droplets inside a Mie image R [-]
n^R	droplet density number of a Mie image R [$1/cm^2$]
$\bar{n}$	mean surface density number [$1/cm^2$]
$\bar{n}_l$	equivalent density number [$1/cm^3$]
r_F	flame radius [μm]
Re	Reynolds number [-]
Sc	Schmidt number [-]
$SD[D_i]$	standard deviation of the inter-droplet distance [μm]
X	longitudinal coordinate in the mid-plane [mm]
Y	vertical coordinate in the mid-plane [mm]
Z	transversal coordinate [mm]
α	slope coefficient for the mean inter-droplet distance [-]
β	slope coefficient for the standard deviation of the mean inter-droplet distance [-]
ϵ	thickness of the laser sheet [mm]

References

[1] Godsave, G. A. E., 1953, 4th Symp. on Combustion/The Comb. Institute.
[2] Spalding, D. B., 1953, 4th Symp. on Combustion/The Comb. Institute.
[3] Annamalai, K., and Ryan, W., 1992, *Prog. in Energy and Combustion Science,* 18, pp. 221-295.
[4] Chiu, H. H., and Kim, H. Y., and Croke, E. J., 1982, 19th Symp on Combustion/The Comb. Institute.
[5] Correa, S. M., and Sichel, M., 1982, 19th Symp on Combustion/The Comb. Institute.
[6] Kerstein, A. R., and Law, C. K., 1982, 19th Symp on Combustion/The Comb. Institute.
[7] Candel, S., and Lacas, F., and Darabiha, N., and Rolon, J. C., 1999, *Multiphase Science and Technology,* 11, pp. 1-18.
[8] Borghi, R., and Champion, M., 2000, "Modélisation et théorie des flammes". Ed. Technip.
[9] Réveillon, J., and Vervisch, L., 2005, *Journal of Fluid Mechanics,* 537, pp. 317-347.
[10] Elperin, T., and Krasovitov, B., 1994, *Atomization and Sprays.,* 4, pp. 79-97.
[11] McDonell, V. G., and Adachi, M., and Samuelsen, G. S., 1992, *Combustion Science and Tech.,* 82, pp. 225-248.
[12] Akamatsu, F., and Mizutani, Y., and Katsuki, M., and Tsushima, S., and Dae Cho, Y., 1996, 26th Symp on Combustion/The Comb. Institute.
[13] Hwang, S. M., and Akamatsu, F., and Park, H.-S., 2007, *J. Ind. Eng. Chem.,* 13, pp. 206-213.
[14] Beck, C. H., and Koch, R., and Bauer, H.-J., 2008, *J. of Eng. for Gas Turbines and Power,* 130, pp. 1-8.
[15] Beck, C. H., and Koch, R., and Bauer, H.-J., 2009, 32th Symp on Combustion/The Comb. Institute.
[16] Lovett, J.A. et al., 2014, *J. of Eng. for Gas Turbines and Power,* 136, Nr.041503.
[17] Vicentini, M., and Lecourt, R., and Bodoc, V., and Rouzaud, O., and Simonin, O., 2014, Proceedings of the Congrès Francophone des Techniques Laser.
[18] Vicentini, M. et al., 2015, 6th European Conf. for Aeronautics and Space Sciences.
[19] Crowe, C. T., and Schwarzkopf, J. D., and Sommerfeld, M., and Tsuji, Y., 2011, "Multiphase flows with droplets and particles". CRC Press.
[20] Chandrasekhar, S., 1943, *Review of Modern Physics,* 15, pp. 1-89.
[21] Neumann, P., and Umbauer, H., 1991, *Experiments in Fluids,* 12, pp. 81-89.
[22] Vicentini, M., 2016, Ph.D. Thesis to be presented, June 2016.